21st IAEA Fusion Energy Conference
Chengdu, China Oct. 16-21, 2006

DEPENDENCE OF THE H-MODE PEDESTAL STRUCTURE ON ASPECT RATIO

R. Maingi[1], A. Kirk[2], T. Osborne[3], P. Snyder[3], S. Saarelma[2], R. Scannell[2], B.P. LeBlanc[4], H. Meyer[2] and the DIII-D, MAST and NSTX research teams

1) Oak Ridge National Laboratory, Oak Ridge TN, 37831 USA
2) UKAEA Fusion, Culham UK
3) General Atomics, San Diego CA USA
4) Princeton Plasma Physics Lab, Princeton NJ USA

This page intentionally left blank

Dependence of the H-mode Pedestal Structure on Aspect Ratio

R. Maingi[1], A. Kirk[2], T. Osborne[3], P. Snyder[3], S. Saarelma[2], R. Scannell[2], B.P. LeBlanc[4], H. Meyer[2] and the DIII-D, MAST and NSTX research teams
(email: rmaingi@pppl.gov)
[1] *Oak Ridge National Laboratory, Oak Ridge TN USA*
[2] *UKAEA Culham, Culham, U.K.*
[3] *General Atomics, San Diego CA USA*
[4] *Princeton Plasma Physics Laboratory, Princeton NJ 08543 USA*

Abstract. We report on the progress of a set of experiments between DIII-D, MAST, and NSTX to determine the aspect ratio dependence of the pedestal. The pedestal-top electron collisionality $\nu_e^* \sim 1$ was matched in all three devices, as was the pedestal-top normalized ion gyroradius $\rho_i^* \sim 0.015$. The goal of this set of experiments is to assess the pedestal widths and gradients, as well as the edge stability of each set of discharges. While substantial progress has been made toward this goal, the final answer awaits further analysis. The status of experiments and analysis on each machine is therefore described.

I. Introduction

An accurate prediction of the H-mode pedestal parameters is key in performance projections for the International Thermonuclear Experimental Reactor (ITER). High pedestal temperature appears to be necessary to achieve sufficient core energy confinement. However ideal magnetohydrodynamic (MHD) stability appears to set the maximum edge pressure gradient in the pedestal before large edge-localized modes (ELMs) are encountered[1]. Explicit determination of the dependence of the pedestal heights, widths, and gradients on the device inverse aspect ratio (ε = a/R) has recently received attention,

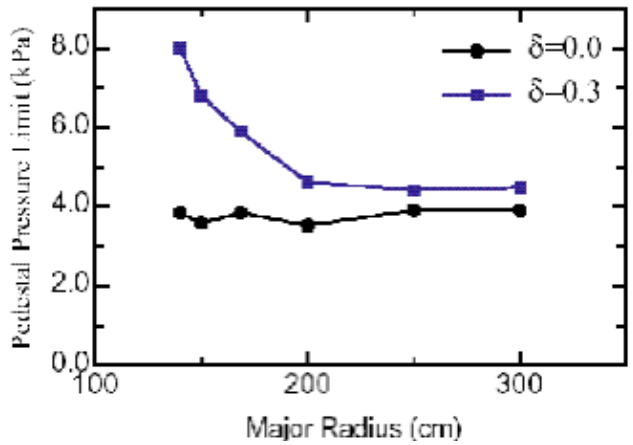

Fig. 1. Dependence of pedestal pressure limit in major radius at a fixed minor radius of 0.603m, i.e. an aspect ratio scan[6].

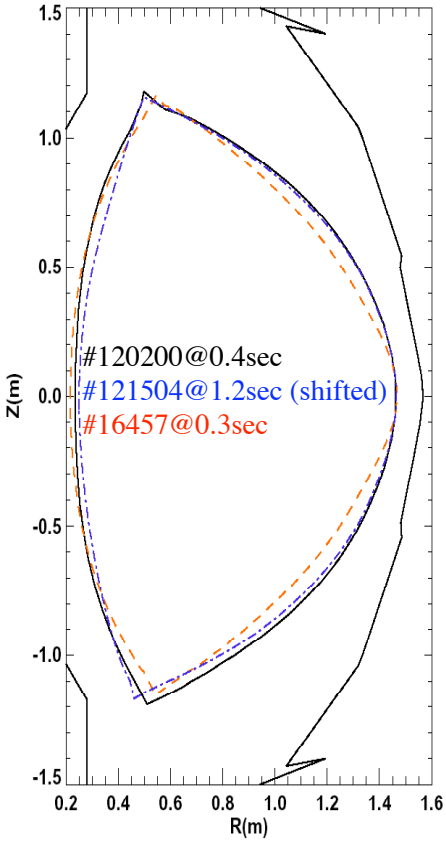

Fig. 2. Common double-null shape developed for aspect ratio scan. Color code: NSTX (black), MAST (red: dashed), and DIII-D (blue: dash-dot). The DIII-D shape was shifted inward by 0.82m.

because many of the machines in the international database used for scaling to ITER have different aspect ratios. In this regard, a strong dependence of the pedestal on aspect ratio would not be surprising, because variation of the aspect ratio primarily affects the edge magnetic topology. Determination of the effect of aspect ratio can take the form of an explicit aspect ratio term in the pedestal scaling[2], or a multi-machine comparison as discussed here.

Previous studies have suggested the possibility of a strong aspect ratio dependence of the pedestal. For example, a scaling study of the H-mode T_e pedestal width (Δ_{Te}) involving DIII-D and JT-60U showed clear differences in the pedestals, implying $\Delta_{Te} \sim \varepsilon^{0.5}$ if solely attributed to the aspect ratio difference[3]. More recently, stability calculations with the ELITE code[4, 5] rather robustly showed that the pedestal pressure was expected to increase with decreasing major radius at moderate shaping, i.e. triangularity $\delta \sim 0.3$-0.4 (Figure 1)[6]. This calculation was done assuming a fixed pedestal width, so that the prediction is effectively of the critical pedestal gradient. Since the minor radius was held constant, the aspect ratio decreased with decreasing major radius. Thus the calculations imply an increase of the pedestal pressure gradient with inverse aspect ratio. Other fixed quantities in this calculation were plasma current I_p, toroidal field B_t, and density; the pedestal T_e (P_e) and gradient were varied until the onset of the peeling/ballooning instability. Note that this prescription for locating the peeling/ballooning boundary produces a decreasing electron collisionality ν_e^* along the x-axis of Figure 1 because[7] $\nu_e^* \sim T_e^{-2} \varepsilon^{-1.5}$.

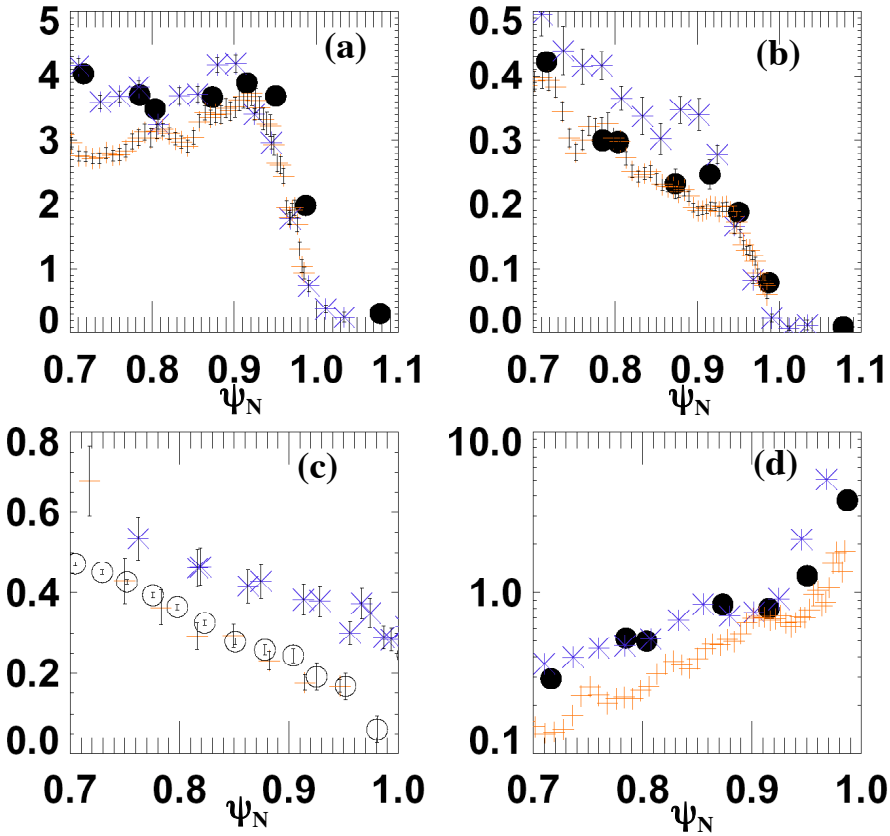

Fig. 3. Profiles from DIII-D (blue stars - #121504@1.175 sec.), MAST (red crosses - #16457@0.33 sec.), and NSTX (black circles - #120200@0.365 sec.) for: (a) n_e, [10^{19} m^{-3}], (b) T_e [keV], (c) T_i [keV], (d) ν_e^*. The pedestal top in DIII-D, MAST and NSTX occurs at ~ $\psi_N \sim 0.9$, 0.95 and 0.95 for DIII-D, MAST, and NSTX respectively. Note that panels (a) and (b) extend radially further than panels (c) and (d). The n_e and T_e data from NSTX are from preliminary calibrations.

With their similar plasma minor radii, MAST, NSTX and DIII-D together provide the opportunity to test this prediction, with the first two machines providing a low aspect ratio comparison with $\varepsilon \sim 0.7$, as compared with the DIII-D $\varepsilon \sim 0.35$. We note that the actual NSTX

and MAST major radii lie to the left of the x-axis in Figure 1, leading to the prospect of a measurably large difference in the pressure gradient limit before the onset of intermediate-n peeling/ballooning modes.

II. Status of experiments

To test the ELITE code prediction discussed above, a common double-null shape was developed for these experiments within each machine. This shape had minor radius ~ 0.61m, triangularity δ~0.5, and elongation κ~1.9, and is shown in Figure 2. There are some minor, residual differences in the shapes between the three devices. In particular, the squareness[8] varied from about 0.0 to 0.2 between MAST and NSTX, with MAST having the lower squareness value. This difference in squareness was concluded to have little impact on the edge stability for this set of experiments: the shape flexibility of DIII-D was used to verify that a squareness variation from 0 to 0.2 had no substantial impact on the plasma profiles within that device in this regime. The toroidal fields and plasma currents used were 0.45-0.55 T and 0.6–0.8 MA in all three machines.

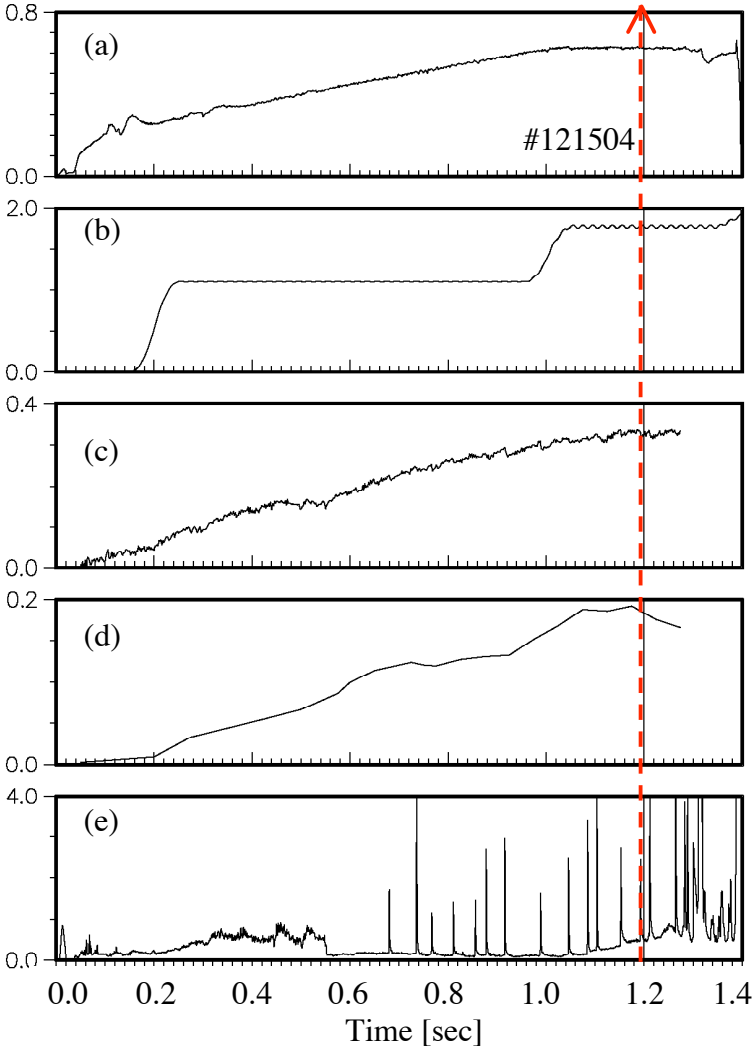

Fig. 4. Characteristics of DIII-D discharge: (a) I_p [MA], (b) neutral beam power P_{NBI}, [MW], (c) line average density n_e [10^{20} m^{-3}], (d) stored energy W_{MHD} [MJ], and (e) divertor D_α [au]. The analysis window was +/- 0.05 sec around the red line.

Generally speaking, the plasma profiles obtained in all three machines were similar (Figure 3). The dimensionless electron collisionality parameter ν_e^* was nonetheless well-matched at the top of the outboard pedestal by variation of the target density while maintaining ELMy H-mode (panel 3d). The normalized ion gyro-radius ρ_i^*~0.015 was also matched at the top of the outboard pedestal between the three devices. Note that the 1/R falloff of the toroidal field means that the toroidal field at the outboard pedestal in DIII-D was ~ 0.45 T, i.e. higher than the 0.29 T in MAST and NSTX. Hence the match in ρ_i^* required that the DIII-D pedestal T_i be higher than in MAST and NSTX. The outboard pedestal values were chosen as the quantities to be matched because ballooning stability imposes the most stringent limits on the local gradients at the low-field

side, i.e. the outer midplane. We note that no attempt was made to match q95, because one of the main manifestations of low aspect ratio is a higher safety factor for comparable I_p and B_t.

IIa. DIII-D results

In order to keep the ion gyro-radius approximately constant across machines, the DIII-D discharges were run at a reduced B_t level of 0.52 T; this was the lowest B_t value that allowed reproducible discharges. The I_p value of 0.6 MA was selected to yield a more comparable |B| across machines at the outer midplane, although as noted above the DIII-D value for |B| was higher than in MAST and NSTX.

Table I: Pedestal characteristics in DIII-D, obtained from the hyperbolic tangent fits

Profile	Height	Width (% of ψ_N)	Peak Gradient
n_e	0.36 (10^{20} m^{-3})	6.3	5.2 (10^{20} m^{-3}/ψ_N)
T_e	0.33 (keV)	8.5	4.2 (keV/ψ_N)
P_e	1.9 (kPa)	6.6	29 (kPa/ψ_N)

Time traces of the main characteristics of a DIII-D discharge from this experiment are show in Figure 4. The L-H transition was observed at t=0.55sec, resulting in an ELMy H-mode discharge. At t=1.0 sec., the neutral beam power P_{NBI} was increased to ~ 1.8 MW to push toward the stability limit. The boundary shape was matched reasonably well, and the discharge was quasi-steady during the analysis time window of t=1.15-1.25 sec.

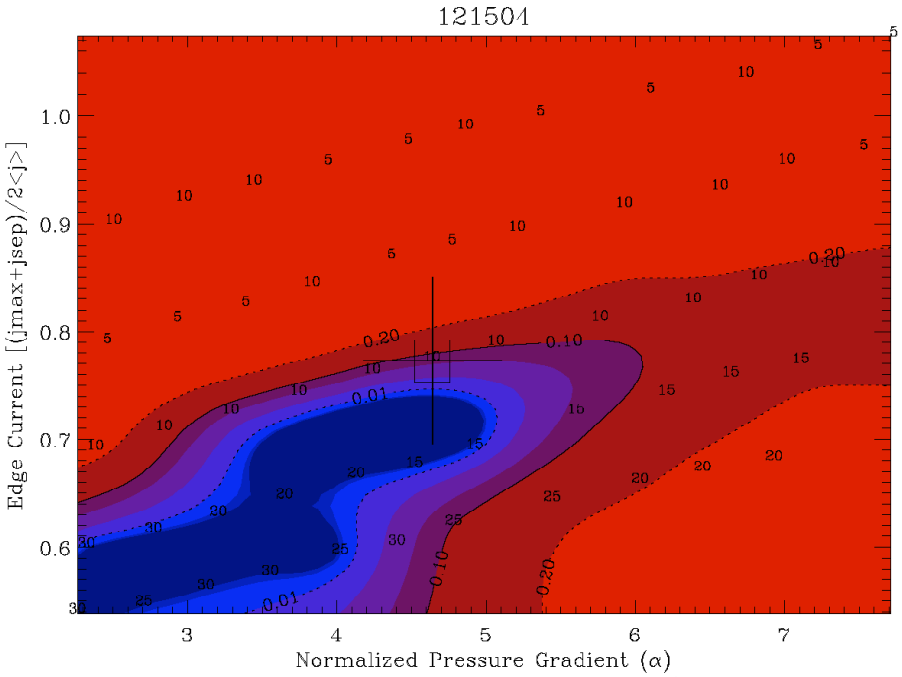

Fig. 5. Results of edge stability calculations for the DIII-D discharge, showing that the edge bootstrap current lies close to the peeling mode stability boundary, indicated by the purple region. The most unstable mode number is indicated by the small numbers. DIII-D discharges from this experiment with slightly higher collisionality lie closer to the ballooning mode boundary than the peeling mode boundary.

The procedure to analyze the edge stability has been described elsewhere[9] and is summarized here. This procedure consists of three parts: step 1 consists of equilibrium reconstruction using the kinetic profiles for constraints within the EFIT reconstruction code[10]. Here n_e, T_e, and P_e profiles are available from a 160 Hz, 40-channel Thomson Scattering system, and T_i profiles from a 100 Hz charge exchange recombination

spectroscopy system. Only the kinetic profiles occurring over the last 20% of the ELM cycles in the analysis window are used as the basis for the equilibrium fits. These profiles (except T_i, which does not exhibit a pedestal structure) were fit with a modified hyperbolic tangent procedure[11]. The P_i profile consists of two parts: the deuteron density profile (obtained from n_e and Z_{eff} profiles, assuming carbon as the dominant impurity) and the carbon pressure profile measured directly by the charge exchange system. The bootstrap current was obtained from a neoclassical calculation using these fitted profiles.

We note that the pedestal n_e, T_e and P_e widths measured for these discharges were between 6-8% in ψ_N (normalized poloidal flux), i.e. almost twice as large as the normal range of widths at the normal B_t=2.1 T (see Table I). Step 2 consists of a variation of the edge pressure gradient (at fixed current density) and the edge current density (at fixed pressure gradient) in a fixed-boundary calculation starting from step #1. Finally step 3 involves evaluation of the edge stability of the equilibria from step #2 with the ELITE code.

Figure 5 shows that the discharge experimental edge current density and normalized pressure gradient were rather close to the peeling mode instability boundary for the discharge in Figure 3. More specifically Figure 5 shows a contour plot of the normalized growth rate (γ/ω_A) for toroidal mode numbers n=5,10,15,20,25,30 computed with the ELITE code, and the reference point is given by the symbol with 10% error bars. The solid line marks the contour of γ/ω_A =0.1, which is a reasonable estimate of the effective stability boundary where $\gamma > \omega_*/2$. Roughly speaking, the blue region is stable, and the shades of purple are the transition region to instability. The small numbers on the plot indicate most unstable mode. This result is consistent with other DIII-D analysis which shows that the edge plasma is near either the peeling or ballooning boundary shortly before a Type I ELM[6].

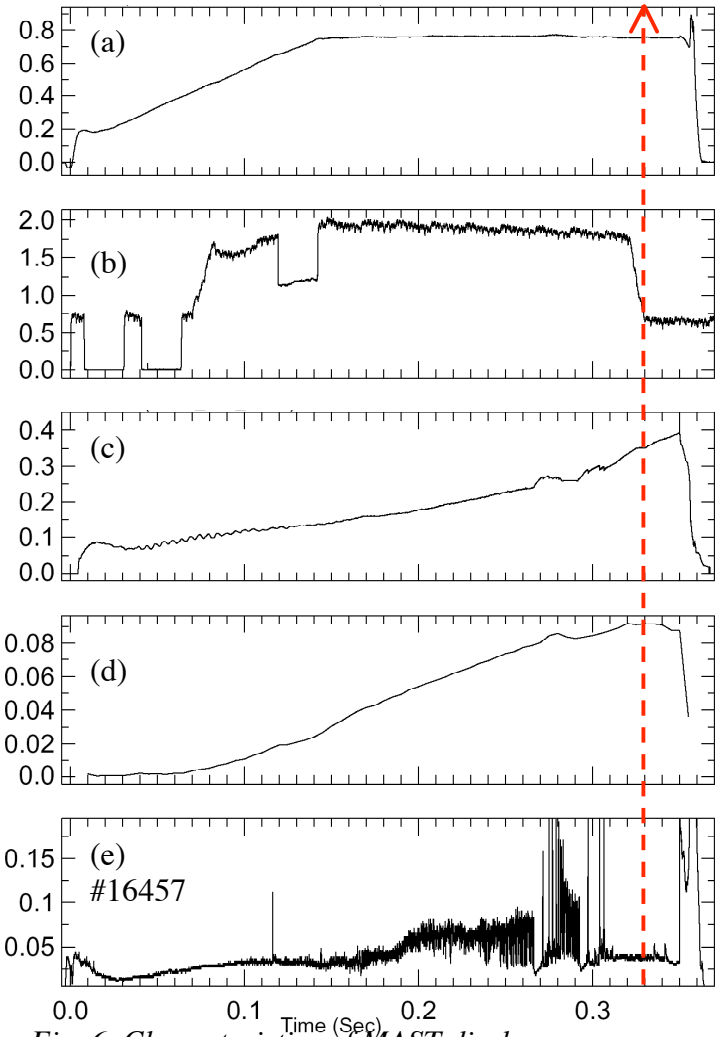

Fig. 6. Characteristics of MAST discharge: (a) I_p[MA], (b) neutral beam power P_{NBI}, [MW], (c) line average density $n_e[10^{20}\ m^{-3}]$, (d) stored energy W_{MHD}[MJ], and (e) divertor D_α[au]. The Ruby laser firing time is given by the red line.

IIb. MAST results

Time traces of the main characteristics of a MAST discharge from this experiment are show in Figure 6. The L-H transition was observed at t=0.265sec, resulting in an ELMy H-mode discharge which subsequently became ELM-free past ~ 0.31 sec. NBI power of 1.9 MW was used.

On MAST, two Thomson scattering systems are installed: a Ruby laser system with 300 channels at a single time slice[12], and a Nd-YaG laser system at 200 Hz which was recently upgraded to 35 channels. The pedestal widths in MAST are obtained from a fit to a hyperbolic tangent function as described above[11], with the extra consideration of the spatial resolution of the diagnostic. This high resolution system has enabled the investigation of various issues, such as the inboard/outboard mapping of pedestal widths[13]. For the subsequent pedestal analysis, we use the 300 channel system (at t=0.33 sec) for optimum spatial resolution, with the pedestal widths obtained from fits of the high-field side data for technical reasons.

In contrast to the broad pedestal widths measured in the DIII-D discharges, the pedestal widths in MAST were measured at between 3.6-4.4% in ψ_N space; the n_e, T_e, and P_e widths were all comparable (Table II). Note that the heights and gradients for n_e and P_e were increased by 25% relative to Figure 3 to account for the ELM free period as explained below.

Table II: Pedestal characteristics in MAST, obtained from the hyperbolic tangent fits

Profile	Height	Width (% of ψ_N)	Peak Gradient
n_e	0.49 +/- 0.13 (10^{20} m^{-3})	4.6 +/- 0.4	11 +/- 0.4 (10^{20} m^{-3}/ψ_N)
T_e	0.16 +/- .006 (keV)	3.6 +/- 0.7	3.8 +/- 1.1 (keV/ψ_N)
P_e	1.4 +/- .06 (kPa)	4.2 +/- 0.4	34 +/- 2.5 (kPa/ψ_N)

The edge stability analysis procedure is similar to that described above for DIII-D, with the ELITE code being the common element. An adjustment is required to the profiles because the time of the Ruby laser firing is almost 20ms before the large ELM that terminates the discharge. The more frequent YaG system profiles show that the n_e and P_e pedestal heights continue to increase by about 25% before the large event near t=0.35 sec; both the n_e and P_e widths, as well as the T_e pedestal height and width, remain relatively constant during that time. Hence the Ruby profiles are n_e and P_e heights and gradients were

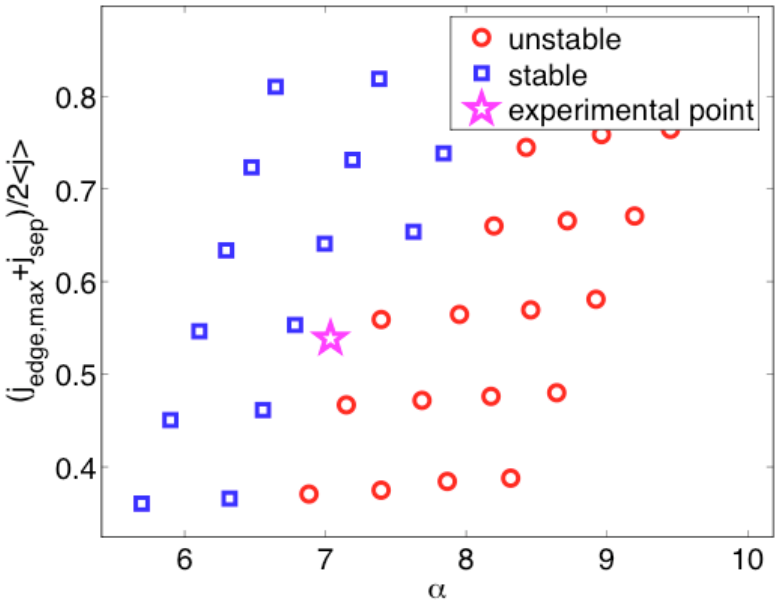

Fig. 7. Results of edge stability calculations for the MAST discharge. The experimental data-point is close to the ballooning boundary.

increased by 25% to account for the pedestal evolution. In addition, it was assumed that the ion pressure gradient was the same as the electron pressure gradient because of the lack of T_i data in the steep gradient region (Fig. 3). Figure 7 shows that the discharge was rather close to the ballooning mode boundary, and well away from the peeling mode stability boundary, i.e. the edge current density would have to increase by at least 100% to destabilize peeling modes.

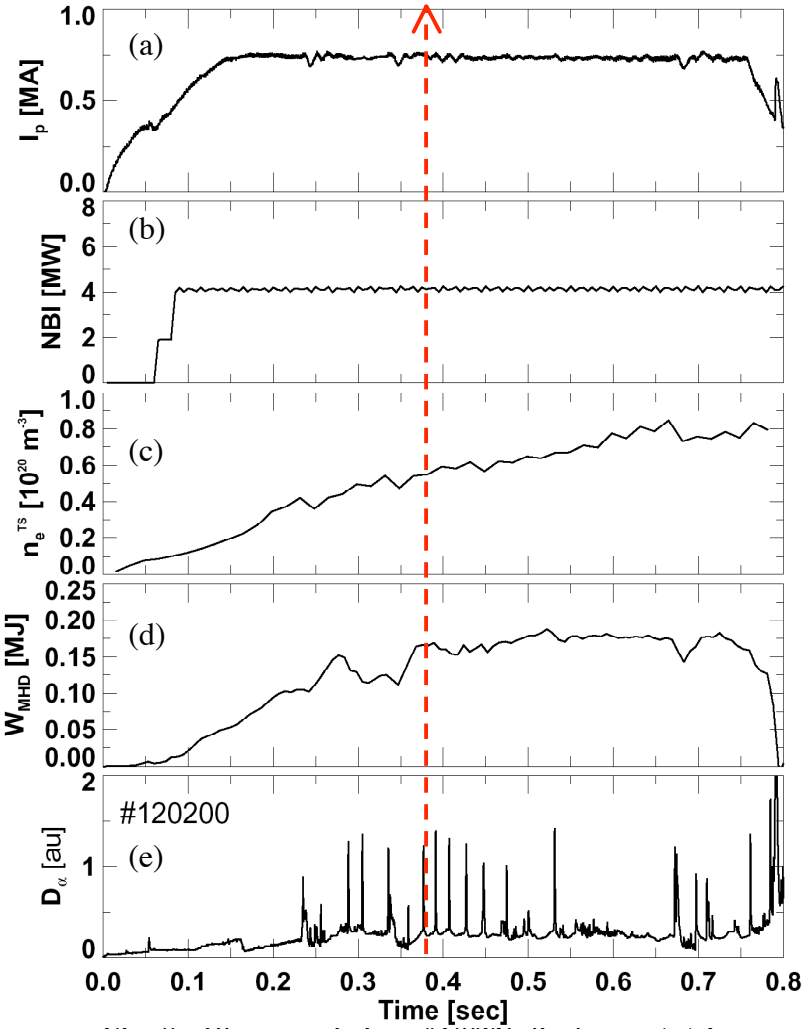

Fig. 8. Characteristics of NSTX discharge:(a) I_p [MA], (b) neutral beam power P_{NBI}, [MW], (c) line average density n_e [10^{20} m^{-3}], (d) stored energy W_{MHD} [kJ], and (e) divertor D_α [au]. The analysis window is +/- 17ms around the red line.

IIc. NSTX results

Time traces of the main characteristics of an NSTX discharge from this experiment are shown in Figure 8. The L-H transition was observed at t=0.165sec, resulting in a Type I ELMy H-mode discharge. A secular density rise is observed in panel (c), a common characteristic of H-mode discharges in NSTX, which originates mainly from the absence of active divertor pumping. This rapid density rise necessitated a higher NBI power of 4 MW to achieve the target ν_e^*.

Evaluation of the profile heights and widths is accomplished with a modified hyperbolic tangent procedure[11] similar to that mentioned above for DIII-D and MAST. The assessment of the n_e, T_e, and P_e heights, widths and gradients from the NSTX discharge were obtained from three Thomson profiles at t=0.365, 0.381, and 0.398 sec. Table III shows that the widths (peak gradients) are smaller (larger) than both DIII-D and MAST. These results are considered preliminary, however, as the final calibrations are in progress. The profile-constrained kinetic equilibrium fits and the subsequent stability analysis will follow.

Table III: Pedestal characteristics in NSTX, obtained from the hyperbolic tangent fits

Profile	Height	Width (% of ψ_N)	Peak Gradient
n_e	0.45 (10^{20} m^{-3})	3.6	10.9 (10^{20} m$^{-3}/\psi_N$)
T_e	0.18 (keV)	1.8	7.6 (keV/ψ_N)
P_e	1.3 (kPa)	2.1	55 (kPa/ψ_N)

III. Summary

We have obtained data in the target shapes in devices in ELMy H-mode discharges. In DIII-D, the pedestal width corresponds to 6-8% of ψ_N, which is ~ 50-100% larger than typical pedestal widths at higher field. The edge stability analysis indicates the plasma is at the peeling/ballooning boundary just before a Type I ELM. In MAST, the pedestal widths measured on the inboard side correspond to 3-4% of ψ_N, which is comparable to typically observed widths. The peak pressure gradients are comparable from these two devices. The stability analysis in MAST indicates proximity to the ballooning boundary. Finally in NSTX, analysis of preliminary Thomson data indicates smaller widths and larger gradients than in the other two devices. The edge stability in NSTX will be assessed pending final Thomson scattering calibrations.

III. Acknowledgements

This research was supported in part by the U. S. Dept. of Energy under contracts DE-AC05-00OR22725, DE-FC02-04ER54698, and DE-AC02-76CH03073, and the U.K. Engineering and Physical Sciences Research Council. We gratefully acknowledge the contribution of the technical staff and neutral beam operations staff from DIII-D, MAST, and NSTX. In addition, we acknowledge the valuable discussion and support from the ITPA pedestal physics working group.

References

[1] Y. Kamada, A.W. Leonard, G. Bateman, et. al., *Proc. 21st Fusion Energy Conference, Chengdu, China, Oct. 16-21, 2006* (2006) paper IT/P1#3.
[2] J. G. Cordey, et. al., *Nuclear Fusion* **43** (2003) 670.
[3] T. Hatae, et. al., *Plasma Physics Controlled Fusion* **42** (2000) A283.
[4] H. R. Wilson, P.B. Snyder, G.T.A. Huysmans, and R.L. Miller, et. al., *Physics of Plasmas* **9** (2002) 1277.
[5] P. B. Snyder, H. R. Wilson, J. R. Ferron, L. L. Lao, A. W. Leonard, T. H. Osborne, A. D. Turnbull, D. Mossessian, M. Murakami, and X. Q. Xu, et. al., *Physics of Plasmas* **9** (2002) 2037.
[6] P. B. Snyder, H R Wilson, T H Osborne, and A W Leonard, et. al., *Plasma Physics Controlled Fusion* **46** (2004) A131.
[7] O. Sauter, C. Angioni, and Y.R. Lin-Liu, et. al., *Physics of Plasmas* **6** (1999) 2834.
[8] J. R. Ferron, et. al., *Physics of Plasmas* **7** (2000) 1976.
[9] T. H. Osborne, P.B. Snyder, T.E. Evans, et. al., *Proc. 32nd EPS Conference on Plasma Physics and Contr. Fusion, Tarragona, Spain, 27 June - 1 July, 2006* **29C** (2005) P4.012.
[10] L. L. Lao, H. St. John, R.D. Stambaugh, A.G. Kellman, and W. Pfeiffer, et. al., *Nuclear Fusion* **25** (1985) 1611.
[11] R. J. Groebner, et. al., *Plasma Physics Controlled Fusion* **40** (1998) 673.
[12] M. J. Walsh, et. al., *Review of Scientific Instruments* **74** (2003) 1663.
[13] A. Kirk, et. al., *Plasma Physics Controlled Fusion* **46** (2004) A187.

* Sponsored in part by U.S. Dept. of Energy Contracts DE-AC05-00OR22725, DE-FC02-04ER54698, and DE-AC02-76CH03073, and the U.K. Engineering and Physical Sciences Research Council.